JACS
JOURNAL OF THE AMERICAN CHEMICAL SOCIETY
pubs.acs.org/JACS
Article

Pore Space Partition Synthetic Strategy in Imine-linked Multivariate Covalent Organic Frameworks

Mengjie Hao, Yinghui Xie, Ming Lei, Xiaolu Liu, Zhongshan Chen, Hui Yang,* Geoffrey I. N. Waterhouse, Shengqian Ma,* and Xiangke Wang*

Cite This: *J. Am. Chem. Soc.* 2024, 146, 1904−1913

ABSTRACT: Partitioning the pores of covalent organic frameworks (COFs) is an attractive strategy for introducing microporosity and achieving new functionality, but it is technically challenging to achieve. Herein, we report a simple strategy for partitioning the micropores/mesopores of multivariate COFs. Our approach relies on the predesign and synthesis of multicomponent COFs through imine condensation reactions with aldehyde groups anchored in the COF pores, followed by inserting additional symmetric building blocks (with C_2 or C_3 symmetries) as pore partition agents. This approach allowed tetragonal or hexagonal pores to be partitioned into two or three smaller micropores, respectively. The synthesized library of pore-partitioned COFs was then applied for the capture of iodine pollutants (i.e., I_2 and CH_3I). This rich inventory allowed deep exploration of the relationships between the COF adsorbent composition, pore architecture, and adsorption capacity for I_2 and CH_3I capture under wide-ranging conditions. Notably, one of our developed pore-partitioned COFs (COF 3-2P) exhibited greatly enhanced dynamic I_2 and CH_3I adsorption performances compared to its parent COF (COF 3) in breakthrough tests, setting a new benchmark for COF-based adsorbents. Results present an effective design strategy toward functional COFs with tunable pore environments, functions, and properties.

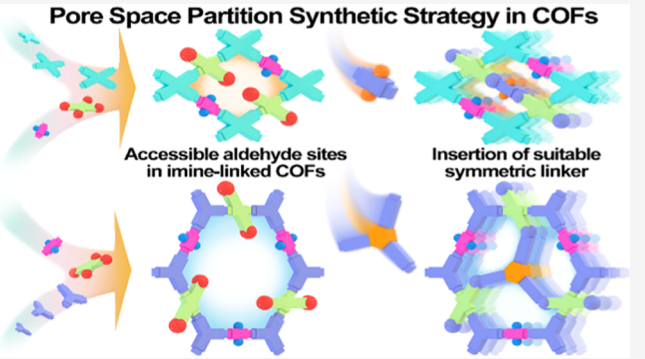

1. INTRODUCTION

Covalent organic frameworks (COFs) are a family of two-dimensional (2D) crystalline porous materials that nowadays find widespread application in environmental remediation,[1,2] light-emitting coatings,[3] catalyses,[4−6] water harvesting,[7,8] gas storage and separation,[9] among others. COFs are attractive for these applications owing to their multifunctionality originating from their programmable design,[10−14] tunable networks of pores and channels,[15,16] and high chemical stability. Over the past 25 years, most COFs have been constructed directly *via de novo* syntheses to introduce predesigned organic functional groups into the pores during the COF synthesis. In addition, some additional functionality can be introduced into COFs through postsynthetic modification strategies.[17−24] These postsynthetic strategies typically involve the introduction of active metal species, different organic constituents, or chemical transformations of functional groups on connecting linkers to impart specific functions. However, postsynthetic modification for tuning the pore space and window size in COFs has received little attention thus far.

From a survey of the field, it is evident that strategies for introducing additional functional units into COF frameworks to partition pores are highly sought after. This would offer a novel approach to achieving control over the pore space, window size, and functionality of COFs. In a recent notable contribution, Xu et al. were able to segment a mesoporous boroxine COF with a fixed pore size of 2.9 nm into six uniform 6.5 Å micropore domains by using a pore partition strategy.[25] However, the challenge of using pore partitioning strategies is the need for precise control over the sites where the additional functional components (pore partition agents) anchor in the channels of the frameworks. Typically, aldehyde or amino groups in the channels of COFs would be used as anchoring points, thereby allowing partitioning of the pore space into multiple smaller domains (e.g., micropores). However, symmetry and size-matching requirements between the parent COF channel and the pore partition agent must be achieved. Accordingly, the application of partitioning strategies to generate pore-partitioned COF materials with well-defined structure−property relationships remains technically challenging.

Received: July 29, 2023
Revised: December 2, 2023
Accepted: December 4, 2023
Published: December 22, 2023

https://doi.org/10.1021/jacs.3c08160
J. Am. Chem. Soc. 2024, 146, 1904−1913

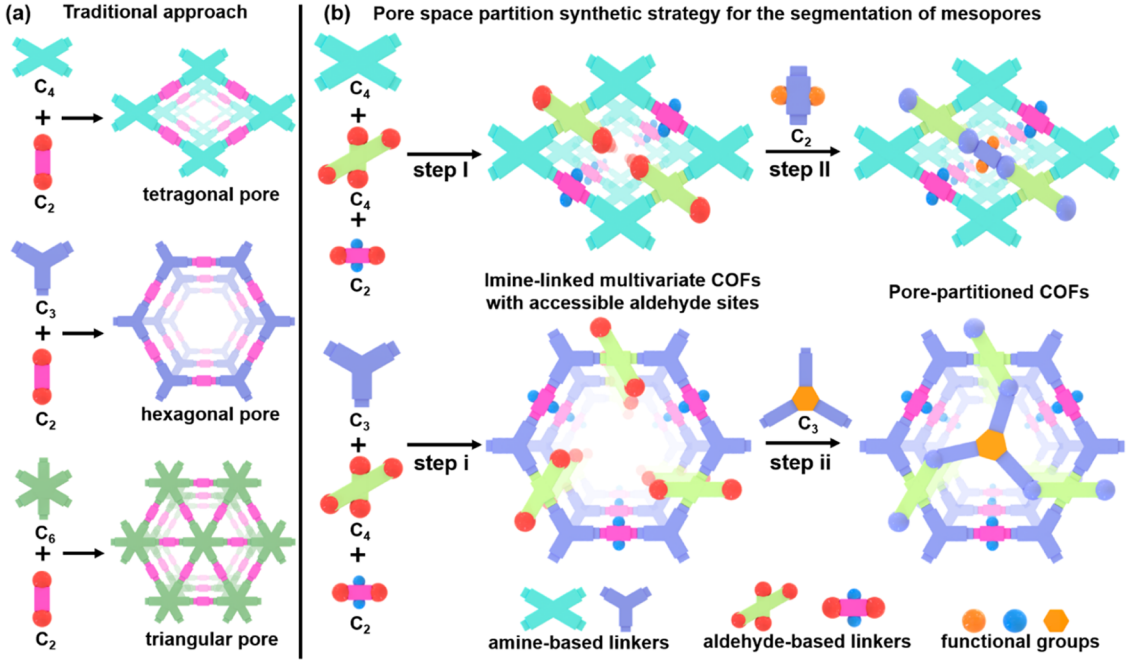

Figure 1. (a) Schematic illustration of the traditional approach used in the synthesis of COFs. (b) Illustration of the pore partition synthetic strategy in imine-linked multivariate COFs, showing the synthesis of multicomponent COFs with predesigned accessible aldehyde sites, followed by the introduction of a symmetric building block as the pore partition agents to divide one micropore/mesopore into two or three micropores.

One of the foremost guiding principles for designing and synthesizing COFs is that of isoreticular chemistry (Figure 1a).[26] This posits that introducing specific components into porous COFs with large pores should allow partitioning into smaller pores while retaining the crystallinity. In this work, we exploit the isoreticular principle to show that large micropores/mesopores of multivariate imine-linked COFs can be partitioned into uniformly interconnected micropores by systematically introducing symmetric linkers as pore partition agents (Figure 1b). We demonstrate that this synthetic strategy can generate diverse libraries of pore-partitioned COF materials, offering a wider range of host−guest interactions for specific applications.

The synthesis of pore-partitioned COF materials involves a two-step process (Figure 1b). First, tetragonal or hexagonal imine-linked COFs were synthesized with aldehyde groups anchored into the channels of the frameworks (Figure 1b, steps (I) and (i)). The large micropores/mesopores in the COFs were then partitioned into uniform smaller micropores by inserting additional linear or triangular linkers as pore partition agents in the center of the pore spaces, producing new pore-partitioned COF materials (Figure 1b, steps (II) and (ii)). We then systematically examined the performance of the parent and pore-partitioned COFs as adsorbents for the capture of I_2 and CH_3I under various conditions. Among the developed COFs, COF 3-2P was identified as a particularly efficient adsorbent for I_2 and CH_3I capture, possessing multi-N components that enabled fast uptake kinetics and a high dynamic uptake capacity of 1.01 and 0.60 g/g, respectively, under the breakthrough condition at 75 °C. Further, COF 3-2P showed a high I_2 and CH_3I uptake capacity of 0.42 and 0.24 g/g at 150 °C (industrially relevant adsorption conditions), respectively. These results demonstrate that pore partitioning allows precise control over the pore environment and functionalities of COF materials, enabling the very challenging capture of iodine-based pollutants. We anticipate that similar pore partitioning strategies will be widely adopted in the future for the design of improved COF-based adsorbents for different applications.

2. RESULTS AND DISCUSSION

2.1. Design, Synthesis, and Characterization of Pore-Partitioned COFs. To implement the pore partitioning protocol, we first synthesized imine-linked COFs with aldehyde sites in the channels. Multicomponent COF 1 was synthesized via an imine condensation of three distinct functional ligands, 4,4′,4″,4‴-(pyrene-1,3,6,8-tetrayl)-tetraaniline (PyTTA), [1,1′:4′,1″-terphenyl]-2′,4,4″,5′-tetracarbaldehyde (TpTTc), and 2,5-pyridinedicarboxaldehyde (PDB) in a solvent mixture of 1,2-dichlorobenzene (o-DCB)/1-butanol (1-BuOH)/acetic acid (AcOH) at 120 °C for 3 days (Figure 2a). The FT-IR spectrum of COF 1 displays a characteristic −C═N stretch at 1620 cm^{-1}, confirming the formation of imine groups (Figures 2b and S1).[27] Notably, the sharp −CHO signal at 1697 cm^{-1} was retained after the formation of COF 1, indicating the retention of aldehyde groups on the TpTTc component (Figures 2b and S1). The solid-state ^{13}C cross-polarization magic-angle spinning (CP-MAS) NMR spectrum of COF 1 showed a −CHO signal at 194.6 ppm, consistent with the FT-IR results (Figure 2c).[25] Powder X-ray diffraction (PXRD) showed that COF 1 possessed a crystalline structure with diffraction peaks at 2θ ~3.8, 7.6, 11.4, 12.3, and 15.2°, which were assigned to the (100), (020), (130), (320), and (330) planes of 2D layers (Figure 2d). Pawley fitting refinement results revealed that the diffraction pattern for COF 1 had unit cell parameters of a = 24.33 Å, b = 24.62 Å, c = 3.97 Å, α = 98.33°, β = 80.35°, and γ = 88.73° with R_p = 1.99% and R_{wp} = 2.50% (Table S1). The experimental result is consistent with an eclipsed (AA) stacking mode constructed by using Material Studio software (Figures 2a,d and S2). The tetragonal pore width and interlayer distance of COF 1 are ~1.1 nm and ~4.0 Å,

https://doi.org/10.1021/jacs.3c08160
J. Am. Chem. Soc. 2024, 146, 1904−1913

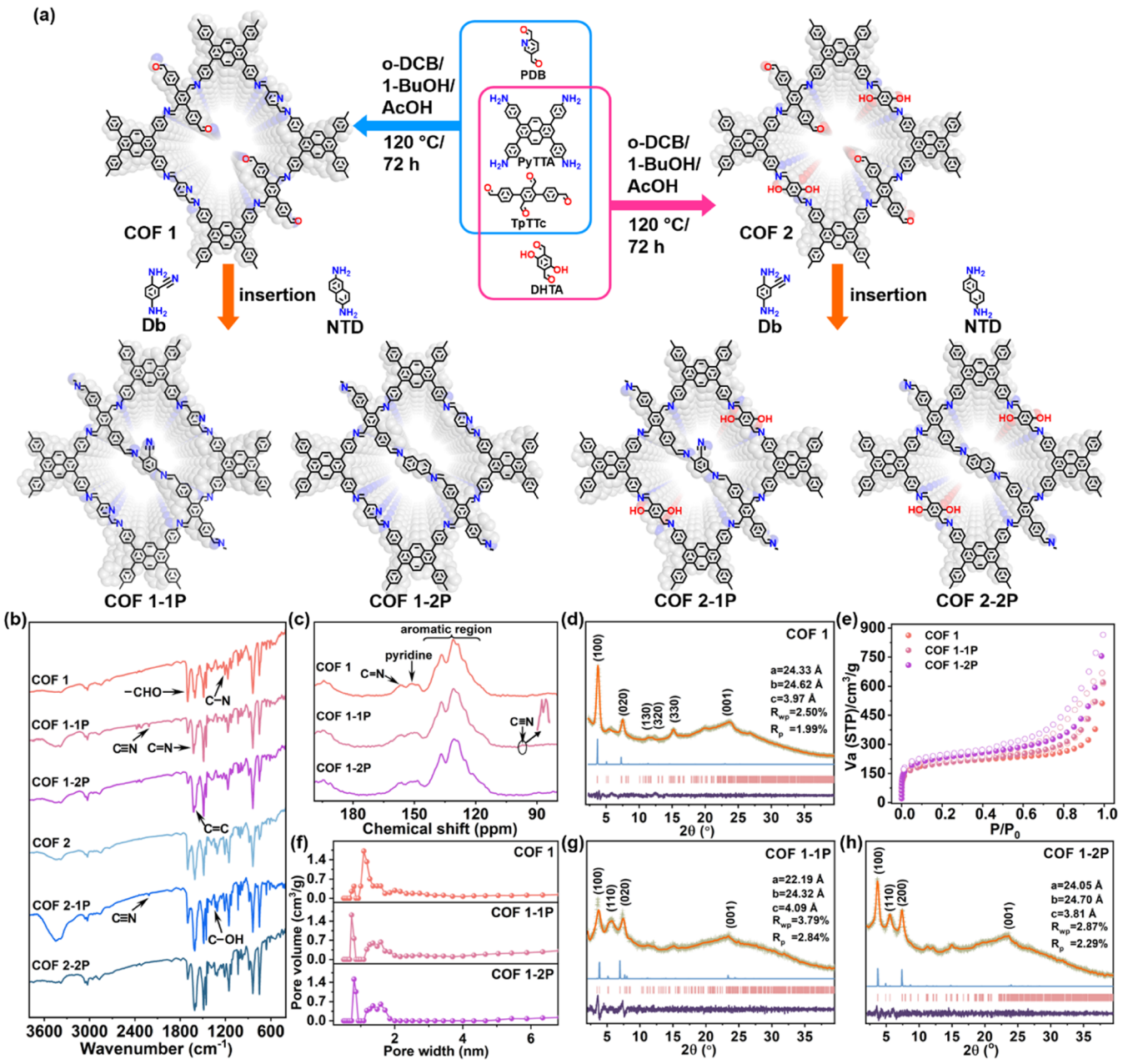

Figure 2. (a) Illustration of the synthesis of COF 1, 1-1P, 1-2P, 2, 2-1P, and 2-2P (the lower figures show the structural model of each COF assuming the AA stacking mode). (b) FT-IR spectra of different COFs. (c) ^{13}C CP-MAS solid-state NMR spectra of COF 1, 1-1P, and 1-2P. (d, g, h) Experimental PXRD patterns of COF 1, 1-1P, and 1-2P with corresponding Pawley refinement (dark orange), simulated results (sky blue), and Bragg positions (brick red) showing good fits to the experimental data (light gray) with minimal differences (dark violet). (e, f) N_2 sorption isotherms and pore size distributions measured at 77 K for COF 1, 1-1P, and 1-2P, respectively.

respectively (Figures 2a and S2). Scanning electron microscopy (SEM) showed that COF 1 possesses a microsphere morphology (Figure S3). The Brunauer−Emmett−Teller (BET) surface area and pore size distribution of COF 1 were determined from the N_2 sorption data at 77 K (Figure 2e,f). Type I adsorption−desorption isotherms with a BET surface area of 643.1 m^2/g were obtained (Table S15). The average pore size was estimated to be ∼1.1 nm using a nonlocal density functional theory (NLDFT) model, consistent with the predicted pore diameter for an AA stacking geometry in the framework (Figure 2f).

The attachment of functional linkers in the channels of COF 1 was expected to tune the pore size and properties. We next partitioned the pore spaces of COF 1 through the introduction of 2,5-diaminobenzonitrile (Db) as a pore partitioning agent. The postsynthetic treatment of COF 1 was carried out in a mixture of mesitylene/1,4-dioxane/AcOH at 120 °C for 3 days. After washing with ethanol and acetone, the obtained powder was denoted as COF 1-1P (Figure 2a). After this treatment, the FT-IR spectrum showed a significant decrease of characteristic −CHO signals at 1697 cm^{-1}, together with the increase of −C═N signals at 1620 cm^{-1} (Figure 2b), suggesting the successful formation of new −C═N bonds through the reaction between aldehyde groups in the channels of COF 1 and amine groups on Db. The presence of the −C≡N stretch at 2214 cm^{-1} after the postsynthetic treatment

https://doi.org/10.1021/jacs.3c08160
J. Am. Chem. Soc. 2024, 146, 1904−1913

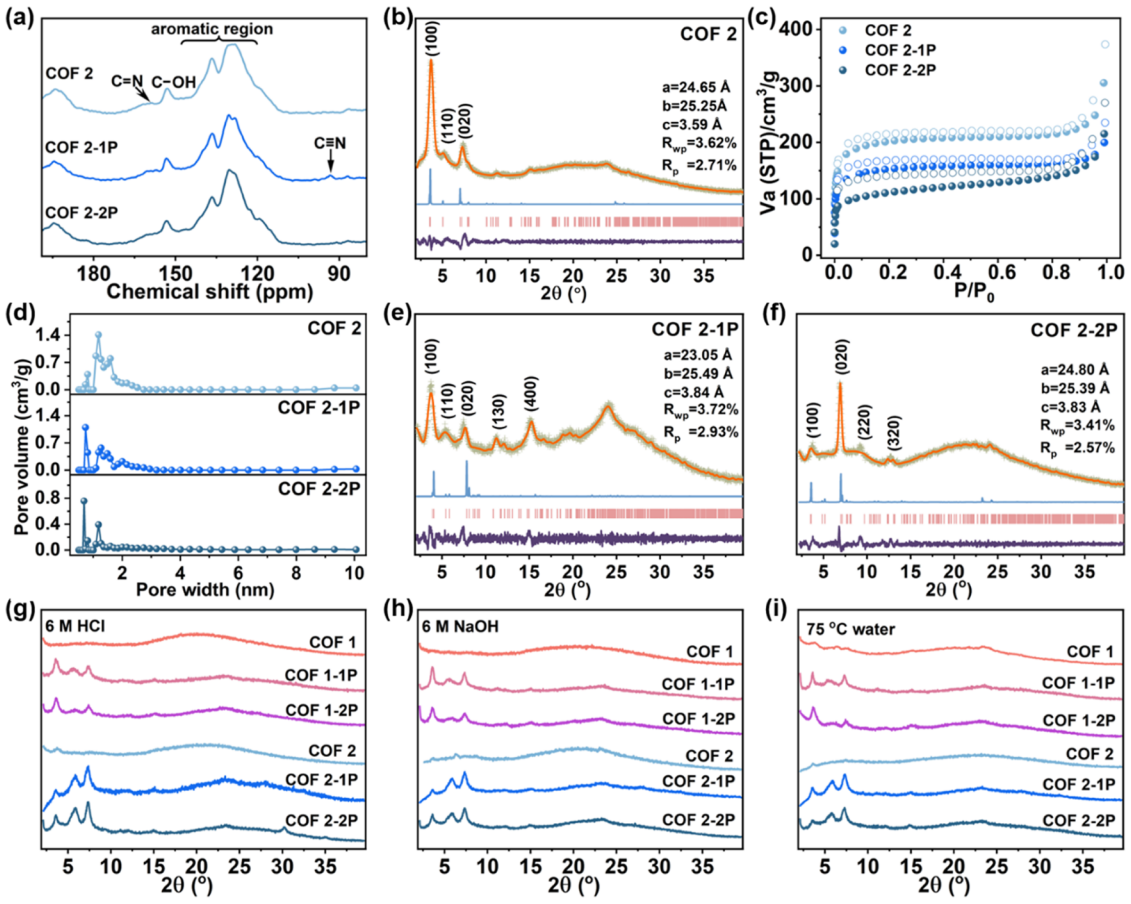

Figure 3. (a) ^{13}C CP-MAS solid-state NMR spectra of COF 2, 2-1P, and 2-2P. (b, e, f) Experimental PXRD patterns of COF 2, 2-1P, and 2-2P with corresponding Pawley refinement (dark orange), simulated results (sky blue), and Bragg positions (brick red) showing good fits to the experimental data (light gray) with minimal differences (dark violet). (c, d) N_2 sorption isotherms and pore size distributions measured at 77 K for COF 2, 2-1P, and 2-2P, respectively. (g–i) PXRD patterns of different COFs after treatment under different conditions.

further confirmed the successful insertion of the Db linker. The solid-state ^{13}C CP-MAS NMR spectrum for COF 1-1P further verified the incorporation of the Db linker, evidenced by the appearance of a new −C≡N signal at 97 ppm (Figure 2c). PXRD confirmed that the crystallinity of the COF was retained after pore space partitioning (Figure 2g). The refined unit cell parameters for COF 1-1P were determined as a = 22.19 Å, b = 24.32 Å, c = 4.09 Å, α = 77.47°, β = 81.28°, and γ = 93.78°, with agreement factors of R_p = 2.84% and R_{wp} = 3.79% (Table S2). Compared with COF 1, the intensity of the (100) reflections of COF 1-1P was weakened relative to the (020) reflections after the pore space partitioning (Figure 2d,g). To better explain how the pore partitioning strategy changes PXRD peak intensities, we calculated the structure factors for selected reflections (Supporting Information, Experimental Procedures section). These calculations revealed that additional electron densities near the unit cell origins contributed positively to negative-valued F_{100}, F_{010}, and F_{110}, resulting in a net reduction of peak intensities (Table S13). Taking these results into account, an eclipsed AA stacking 2D structure with a ∼0.7 nm pore width was obtained, which was obviously smaller than the parent COF 1 (Figures 2a and S2). N_2 adsorption−desorption isotherms allowed the accessible porosity of COF 1-1P to be probed (Figure 2e,f). The pore size distribution analysis verified that pore diameters clustered around 0.7 nm, consistent with the theoretical value from structural simulations (Figures 2f and S2).

On the basis of the aforementioned findings, we conclude that our pore space partition strategy based on the use of a multivariate COF with predesigned aldehyde sites is effective for downsizing the pore sizes. The postsynthetic introduction of amine-based components then serves as pore partition agents, which can be appropriately anchored in the pore center of the parent COF framework through imine linkages to achieve precise pore partitioning. Given these attractive features, we further explored the broader scope of the pore space partition concept and its applicability to the fabrication of other COFs with an elegantly partitioned pore space and enhanced properties. To extend the pore space partition strategy, we next employed 2,6-diaminonaphthalene (NTD) as the pore partitioning agent of COF 1, yielding COF 1-2P (Figure 2a). FT-IR and solid-state ^{13}C CP-MAS NMR spectra confirmed the successful integration of NTD (Figure 2b,c). PXRD and Pawley fitting refined results revealed the crystalline structure of COF 1-2P to be the same as that of COF 1-1P (Figure 2h and Table S3). As expected, the N_2 sorption isotherm for COF 1-2P showed the same type I shape and a similar pore size distribution to COF 1-1P (Figures 2e,f and S2). In addition, we carried out nuclear magnetic resonance (NMR) relaxometry measurements to study the pore environment of the COFs before and after pore space partitioning. Single relaxation peaks were observed for both COF 1 and COF 1-2P, suggesting the single relaxation population present (Figure S4). COF 1-2P showed a single peak at ∼0.066 s,

https://doi.org/10.1021/jacs.3c08160
J. Am. Chem. Soc. 2024, 146, 1904−1913

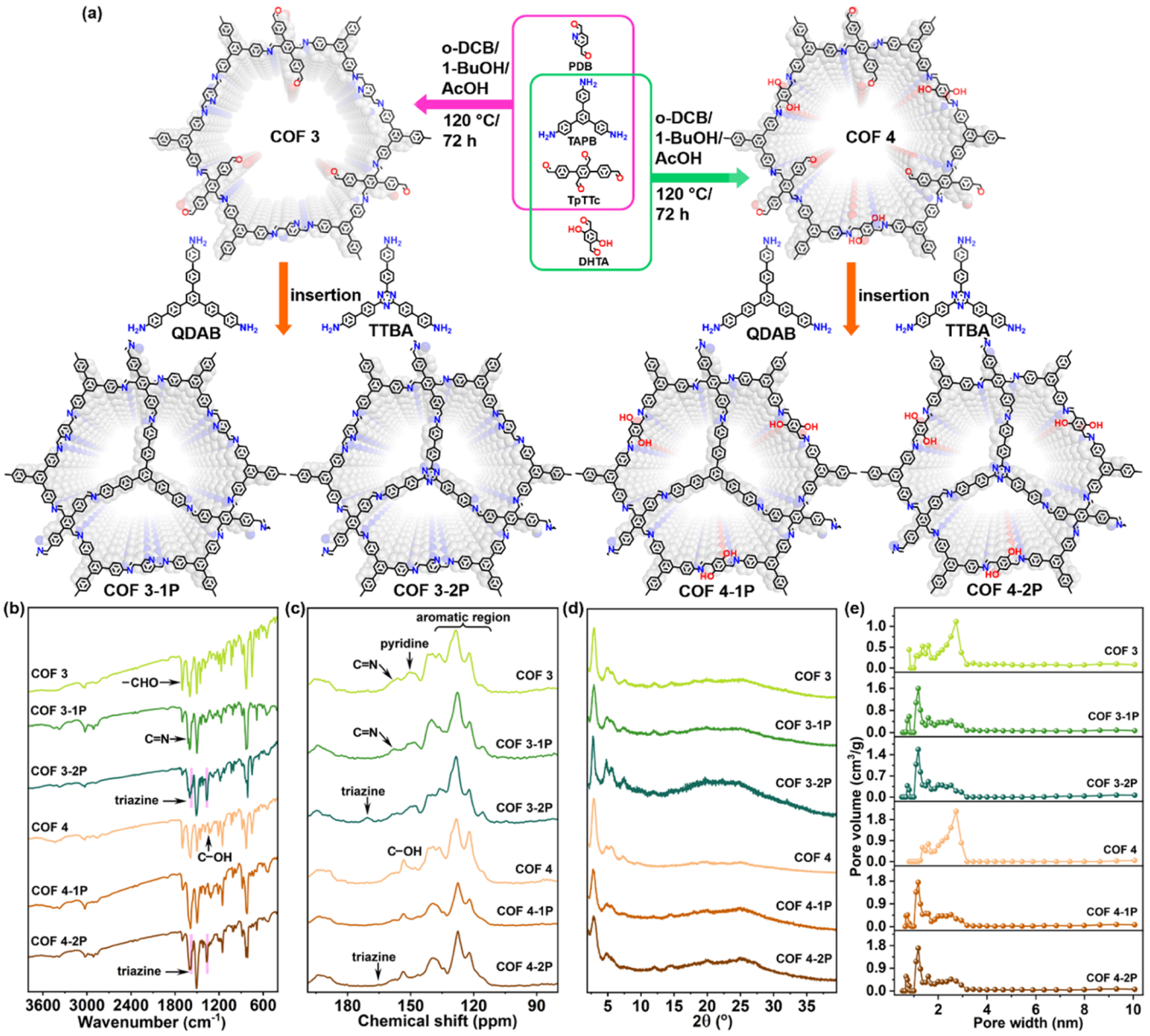

Figure 4. (a) Illustration of the synthesis of COF 3, 3-1P, 3-2P, 4, 4-1P, and 4-2P (the lower figures show the structural model of each COF assuming the AA stacking mode). (b) FT-IR spectra of COF 3, 3-1P, 3-2P, 4, 4-1P, and 4-2P. (c) ^{13}C CP-MAS solid-state NMR spectra of COF 3, 3-1P, 3-2P, 4, 4-1P, and 4-2P. (d) Experimental PXRD patterns of COF 3, 3-1P, 3-2P, 4, 4-1P, and 4-2P. (e) Pore size distributions measured at 77 K for COF 3, 3-1P, 3-2P, 4, 4-1P, and 4-2P.

relatively earlier than that of COF 1 (~0.077 s), indicating that its pore size distribution was smaller than that of COF 1. Moreover, COF 1 and COF 1-2P showed similar signal intensities, suggesting identical amounts of the porous structures. Taken together, the data suggest a near-perfect (almost 100%) insertion of partition agents into the pores of the parent COF.

Encouraged by the results above, we next sought to replace the PDB linker in COF 1 with a hydroxyl-rich linker (2,5-dihydroxyterephthalaldehyde, DHTA), followed by partitioning the tetragonal channels to produce microporous dual hydroxyl and nitrogen-functionalized COFs (Figure 2a). Based on this approach, a hydroxyl functionalized COF was first prepared by combining PyTTA, TpTTc, and DHTA, producing COF 2 with a triclinic unit cell with a = 24.65 Å, b = 25.25 Å, and c = 3.59 Å, $\alpha = \beta = 90°$, and γ = 90.3° (Figures 2a and 3a,b and Table S4). The experimental PXRD pattern closely matched the calculated results based on a model with eclipsed AA stacking (Figure 3b). The solid-state ^{13}C CP/MAS NMR and FT-IR spectra showed the signals at ~153 ppm and ~1334 cm^{-1}, respectively, confirming the presence of hydroxyl groups (C−OH) in the structure (Figures 2b and 3a). The characterization results and calculated unit cell for COF 2 revealed an isoreticular structure similar to that of COF 1.

Subsequently, the tetragonal channels of COF 2 were partitioned into smaller domains by Db and NTD, yielding COF 2-1P and COF 2-2P, respectively (Figure 2a). In comparison with COF 2, the ^{13}C CP/MAS NMR of COF 2-1P showed an additional peak at 93.3 ppm attributed to the −C≡N group from the Db linker (Figure 3a). FT-IR spectroscopy showed characteristic peaks at 1334 cm^{-1} for the COF 2-1P

https://doi.org/10.1021/jacs.3c08160
J. Am. Chem. Soc. 2024, 146, 1904−1913

and COF 2-2P frameworks, confirming the presence of C−OH groups (Figure 2a).[28] PXRD and Pawley refinements reveal that COF 2-1P and COF 2-2P are isoreticular with COF 1-1P and COF 1-2P. All experimental PXRD data were a close match for the calculated data (negligible difference, R_p = 2.93%/R_{wp} = 3.72% for COF 2-1P; R_p = 2.57%/R_{wp} = 3.41% for COF 2-2P), indicating AA stacking mode and phase purity (Figure 3e,f and Tables S5, S6, and S14). In COF 2-1P and COF 2-2P, the hydroxyl groups of the ligand did not affect pore partitioning and caused almost no change in the diameter of the pore width (Figures 3c,d and S5; 1.1 nm for COF 2, and 0.7 nm for both COF 2-1P and COF 2-2P). This indicates that the frameworks can be considered a platform able to tolerate the substitution of functional linkers for broad functionalities without changing the topology.

We then examined the chemical and thermal stabilities of synthesized pore-partitioned COFs. After immersion in HCl, NaOH, and hot water for 12 h, respectively, the COF 1-1P, COF 1-2P, COF 2-1P, and COF 2-2P remained intact with no framework collapse or undesirable phase transitions occurring, as evidenced by the PXRD patterns of the treated COFs being the same with the as-prepared COFs (Figure 3g−i). However, their parent COFs (COFs 1 and 2) showed relatively poor chemical stability under similar conditions. Thermogravimetric analysis (TGA) demonstrated that all pore-partitioned COFs showed slightly better thermal stability than their parent COFs with heating under a nitrogen atmosphere (Figure S6).

To explore the versatility of our synthetic strategy, we subsequently extended the fabrication method to other [C_3 + C_2] COFs (Figures 1b and 4a). COF 3 was synthesized by the imine condensation of 1,3,5-tris(4-aminophenyl)benzene (TAPB), PDB, and TpTTc. COF 4 was prepared via a similar synthetic route, replacing PDB with DHTA. FT-IR, solid-state ^{13}C CP/MAS NMR, PXRD, and Pawley fitting refinement analysis revealed the isoreticular crystalline structures with triclinic unit cells for COF 3 (a = 74.32 Å, b = 76.08 Å, and c = 3.83 Å, α = 92.04°, β = 95.85°, and γ = 121.38°) and COF 4 (a = 72.97 Å, b = 75.47 Å, and c = 3.74 Å, α = 91.48°, β = 85.82°, and γ = 119.59°) (Figures 4b,c and S7 and Tables S7 and S10). The experimental PXRD patterns closely matched the calculated results based on a model with eclipsed AA stacking in both COFs (Figures 4a,d, S7, and S8). The aldehyde groups in the COFs were oriented in an equilateral triangle with three vertices on the TAPB components in both COFs 3 and 4 (Figure 4a). These geometric features allowed the introduction of a C_3-symmetric amine-linker, thus partitioning one pore into three similarly sized micropores. The subsequent postsynthetic reaction of COF 3 or COF 4 with [1,1′:4′,1″:3″,1‴:4‴,1⁗-quinquephenyl]-4,4⁗-diamine, 5″-(4′-amino[1,1′-biphenyl]-4-yl) (QDAB) and 4′,4‴,4⁗′-(1,3,5-triazine-2,4,6-triyl)tris-([1,1′-biphenyl]-4-amine) (TTBA) resulted in the formation of COF 3-1P, COF 3-2P, COF 4-1P, and COF 4-2P, respectively (Figure 4a). The successful synthesis of these pore-partitioned COFs was verified by using a range of experimental techniques. We focus on COF 3-2P as a representative example of the structural description of these materials. The observed signal at 170.5 ppm by solid-state ^{13}C NMR, together with FT-IR peaks 1583 and 1363 cm^{-1}, confirmed the presence of triazine rings in the structure of COF 3-2P (Figure 4b,c), demonstrating successful pore space partitioning by TTBA. The experimental PXRD pattern for COF 3-2P exhibited main diffraction peaks at 2θ ~2.76, 4.81, 5.52, and 7.31°, which could be assigned to the (200), (220), (400), and (420) planes, respectively (Figure S7). Structural modeling and Pawley refinement fitting allowed for the crystal structure to be elucidated. The most probable structure was determined to be a 2D net with AA stacking mode (space group: P1, a = 74.45 Å, b = 75.39 Å, c = 3.77 Å, and α = 101.77°, β = 87.46°, γ = 119.88°; R_p = 2.01% and R_{wp} = 2.53%) (Figures S7 and S8 and Table S9). In addition, the FT-IR, solid-state ^{13}C NMR, PXRD, and Pawley refinement fitting results confirmed that COF 3-1P, COF 3-2P, COF 4-1P, and COF 4-2P were isostructural porous neutral frameworks (Figures 4b−d and S8 and Tables S8, S9, S11, and S12). SEM showed that COFs possess microsphere-like morphologies (Figure S3). COF 3 and COF 4 displayed a combination of type I/IV adsorption/desorption isotherms, indicating the presence of mesoporous structures. After pore segmentation, COF 3-1P, COF 3-2P, COF 4-1P, and COF 4-2P demonstrated type I curves with microporous characteristics (Figure S9). The BET specific surface area for the samples, determined from the N_2 sorption isotherms, ranged from 728 to 1083 m^2/g (Figures S9, S11, and S12 and Table S15). The calculated pore sizes of COF 3-1P, COF 3-2P, COF 4-1P, and COF 4-2P were all ~1.1 nm (Figure 4e), in agreement with the predicted pore diameters for the eclipsed AA geometries (Figure S8). The logarithmic scale of COF 3-1P, COF 3-2P, COF 4-1P, and COF 4-2P showed lower nitrogen uptake than their parents, COF 3 and COF 4, at low relative pressures (~ ranging from 0.001 to 0.01), respectively, suggesting that COFs after pore segmentation have a greater volume of such smaller pores (Figures S9, S11, and S12). NMR relaxometry spectra further revealed that the pore size distribution of COF 3-2P is smaller than that of its pristine COF 3, indicating the successful insertion of the pore partitioning agent (Figure S10). COF 3-1P, COF 3-2P, COF 4-1P, and COF 4-2P showed enhanced chemical and thermal stability compared to those of COF 3 or COF 4, evidenced by their PXRD results (Figure S13). The N_2 adsorption isotherms of those samples showed small amounts of reducing the porosity, further demonstrating the framework stability (Figure S14). The chemical stabilities of COF 3-1P, COF 3-2P, COF 4-1P, and COF 4-2P were better than that of their parent COF 3 and COF 4, respectively, probably due to the inset QDAB and TTBA linkers improving the rigidity of frameworks. Similar strategies have been used and demonstrated the enhanced stabilities in MOF structures.[29−34]

2.2. Iodine and Iodomethane Capture by Pore-Partitioned COFs. The efficient capture of iodine (I_2) and iodomethane (CH_3I) from the off-gas stream of nuclear power plants is challenging and industrially important.[35] Adsorbents such as silver compounds,[36,37] zeolites,[38] metal−organic frameworks,[39−47] and polymers[48,49] have been developed for the capture of these iodine pollutants. However, most of these studies have focused on the adsorption of I_2 vapor and CH_3I in closed systems, whereas only a few studies have addressed the dynamic removal of iodine species. Recently, COFs have attracted interest as potential adsorbents in iodine species adsorptive capture.[50−58] In this context, the pore partitioning methodology presented herein offers an avenue for tailoring the properties of COF-based adsorbents toward I_2 vapor and CH_3I capture. As a proof-of-concept, we conducted experiments to assess the dynamic I_2 vapor and CH_3I adsorption performance of the various pore-partitioned COFs and their parent COFs.

https://doi.org/10.1021/jacs.3c08160
J. Am. Chem. Soc. 2024, 146, 1904−1913

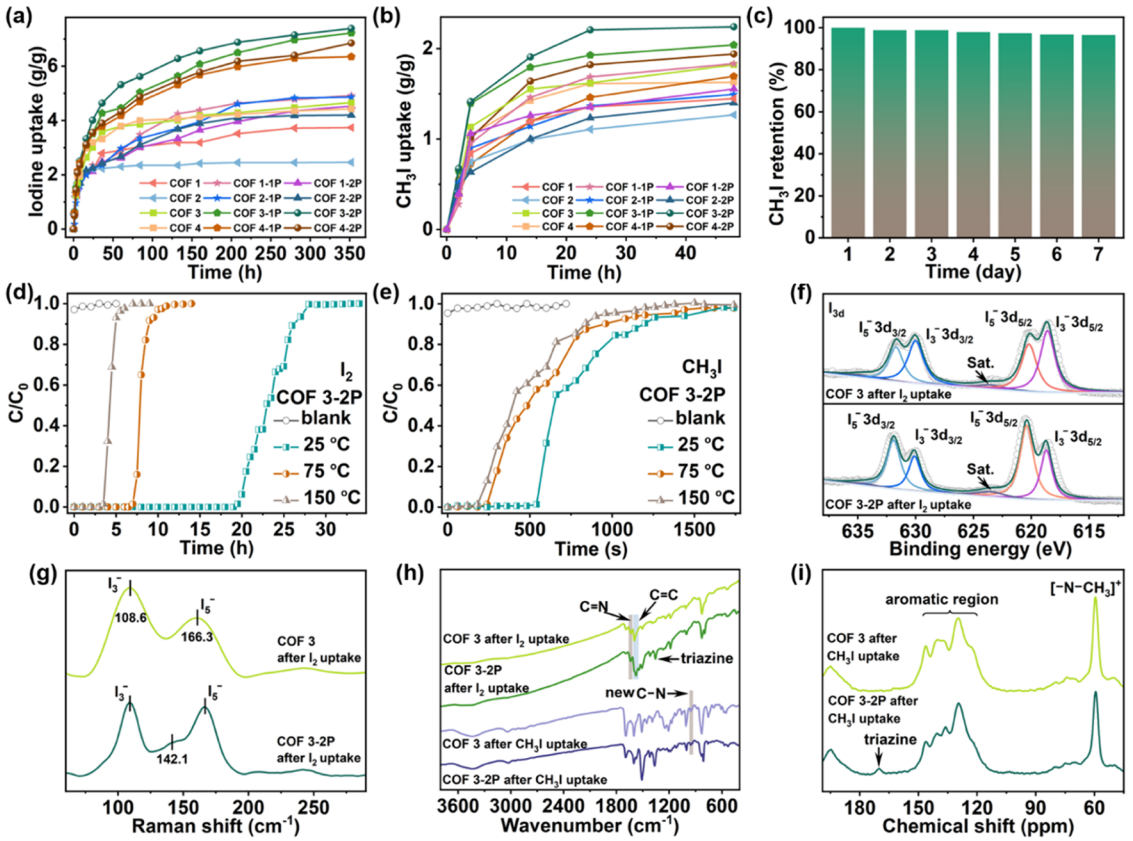

Figure 5. (a) Static I_2 vapor adsorption kinetics on different COFs upon exposure to I_2 vapor at 75 °C. (b) Static CH_3I adsorption kinetics on different COFs upon exposure to CH_3I at 75 °C. (c) Exposure of saturated CH_3I/COF 3-2P to air at 25 °C for 7 days. (d) Experimental column breakthrough curves for I_2 vapor in an absorber bed packed with COF 3-2P. (e) Experimental column breakthrough curves for CH_3I in an absorber bed packed with a COF 3-2P. (f) I 3d XPS spectra of COF 3 and COF 3-2P after the adsorption of I_2. (g) Raman spectra of COF 3 and COF 3-2P after the adsorption of I_2. (h) FT-IR spectra of COF 3 and COF 3-2P after the adsorption of I_2 and CH_3I. (i) ^{13}C CP-MAS solid-state NMR spectra of COF 3 and 3-2P after the adsorption of CH_3I.

We first carried out I_2 and CH_3I adsorption experiments in a static closed system at 75 °C. The adsorption capacity and kinetics are summarized in Figure 5a,b. All of the COFs after pore space partitioning demonstrated higher uptake capacities over their parent COFs. Notably, COF 3-2P displayed relatively fast I_2 adsorption kinetics, with an uptake value reaching ~7.4 g/g over 352 h (Figures 5a and S15 and Table S16). COF 3-1P, COF 4-1P, and COF 4-2P showed slightly lower uptake capacities under similar conditions. When used for CH_3I capture at 75 °C, the adsorption capacity of COF 3-2P was determined to be 2.24 g/g with fast adsorption kinetics, outperforming most other reported adsorbents (Figure 5b and Table S17).[56,58−60] Exposure of the CH_3I-saturated COF (i.e., CH_3I/COF 3-2P) to air at 25 °C for 7 days resulted in negligible weight loss, suggesting a strong host−guest interaction between CH_3I and COF 3-2P (Figure 5c). Moreover, COF 3-2P can be regenerated and recycled with ~40% losses in I_2 adsorption (Figure S16). Given the strong interactions, iodine incorporated into the COF cannot be facilely desorbed with the procedure by rinsing with a solvent or thermal desorption at a high temperature. The results show that COF 3-2P has great potential for the capture of I_2 and CH_3I in gas streams.

Encouraged by the relatively fast kinetics and high adsorption capacity of COF 3-2P, we next performed dynamic I_2 and CH_3I adsorption experiments under breakthrough conditions to simulate the treatment of industrial off-gas streams. COF 3-2P achieved an equilibrium adsorption capacity of 2.42, 1.01, and 0.42 g/g at 25, 75, and 150 °C toward I_2, respectively (Figure 5d and Table S18). As shown in Figure 5e, CH_3I was detected at breakthrough times of approximately 540, 240, and 180 s at 25, 75, and 150 °C, respectively. The calculated dynamic adsorption capacities were 1.06, 0.60, and 0.24 g/g, respectively, higher than most of the other reported adsorbents (Table S19). For comparison, CH_3I was detected after a short breakthrough time in the absence of the COF 3-2P.

After demonstrating the excellent dynamic I_2 and CH_3I adsorption performance of COF 3-2P under wide-ranging conditions, we next sought an in-depth understanding of the I_2 and CH_3I adsorption mechanism by carrying out X-ray photoelectron spectroscopy (XPS), Raman, FT-IR, and solid-state ^{13}C NMR measurements. As shown in Figure 5f, the I 3d XPS spectrum of COF 3 and COF 3-2P after I_2 adsorption experiments could be deconvoluted into two sets of peaks at 618.6 and 630.1 eV (3:2 area ratio) and 620.1 and 631.7 eV (3:2 area ratio), corresponding to I_3^- and I_5^- species, respectively.[58,61] Results suggested the COFs adsorbed iodine in the forms of I_3^- and I_5^-, likely through interactions with the exposed N atoms of the framework.[58,61] The I_5^- signals were more intense relative to the I_3^- signals for COF 3-2P, while the opposite was observed for COF 3, revealing that pore space partitioning by the nitrogen-rich TTBA linker improved iodine uptake performance. These results were consistent with the

https://doi.org/10.1021/jacs.3c08160
J. Am. Chem. Soc. 2024, 146, 1904−1913

adsorption experimental results and helped explain the enhanced I_2 adsorption performance of COF 3-2P. Raman spectroscopy further revealed the existence of I_3^- and I_5^- on the surface of the used COFs (Figure 5g). Compared with the FT-IR spectra of COF 3 and 3-2P, the C═N stretching vibrations shifted from 1620 to 1639 cm^{-1} after I_2 uptake, revealing that exposed N atoms transferred electrons to adsorbed I_2 molecules to form I_3^- and I_5^- (Figure 5h). After CH_3I uptakes, FT-IR spectroscopy of COF 3 and COF 3−2P revealed the formation of new C−N (N^+-CH_3) bonds through methylation, evidenced by the emergence of a new peak at 955 cm^{-1} (Figure 5h).[55,58] Solid-state ^{13}C NMR showed characteristic peaks at ∼59.6 ppm, confirming *N*-methylation (Figure 5i).[56,58] The long breakthrough time and high dynamic capacity suggest that COF 3-2P is a very promising adsorbent for use in packed columns for I_2 and CH_3I capture from the off-gas stream of nuclear power plants.

We next carried out density functional theory (DFT) calculations to better understand the I_2 and CH_3I adsorption mechanisms. On the basis of XPS, Raman, FT-IR, and solid-state ^{13}C NMR results, we considered first I_3^-, I_5^-, and CH_3I binding on the N-containing pyridine, imine, and triazine sites of COF 3−2P. Figure S17 shows models of binding sites, including I_3^-/pyridine, I_5^-/pyridine, I_3^-/imine N, I_5^-/imine N, I_3^-/triazine N, and I_5^-/triazine N of COF 3-2P. The binding free energies of I_3^-/pyridine, I_5^-/pyridine, I_3^-/imine N, I_5^-/imine N, I_3^-/triazine N, and I_5^-/triazine N were calculated to be −0.51, −0.58, −0.45, −0.45, −0.30, and −0.46 eV, respectively. Moreover, the binding free energies of CH_3I/pyridine, CH_3I/imine N, and CH_3I/triazine N were −0.33, −0.24, and −0.22 eV, respectively. These results revealed the efficient contribution of triazine N sites to I_2 and CH_3I adsorption after pore space partitioning by the TTBA linker, suggesting strong binding affinities of triazine N for I_3^-, I_5^-, and CH_3I. This further explains the excellent adsorption of I_2 and CH_3I on COF 3-2P, highlighting the precise control over the pore environment and functionalities of the pore space partition strategy.

Taken together, these experimental results reveal that pore space partitioning can deliver functional multicomponent COFs for specific applications. The pore space partition strategy reported here utilized multivariate COFs with accessible aldehyde sites, allowing the controlled introduction of matching C_3 and C_2 symmetry pore partition agents to divide the 1D tetragonal and hexagonal channels into uniformly sized micropores, thus producing microporous frameworks. By this approach, diverse libraries of pore-partitioned COF materials could be synthesized and screened as high-performance adsorbents for target applications (e.g., the capture of iodine species). We anticipate that our proof-of-concept study will serve as inspiration for the synthesis of improved COF-based adsorbents for selective separations, waste-stream processing, and environmental remediation.

3. CONCLUSIONS

In summary, we have proposed a simple and versatile synthetic strategy for the realization of pore space partitioning in imine-linked covalent organic frameworks. This strategy is applicable for the segmentation of tetragonal or hexagonal pores into multiple uniformly sized micropores. We demonstrated that pore partitioning is a versatile platform for the rational design of COF-based adsorbents for I_2 and CH_3I. Further, this synthetic strategy creates vistas toward functional COFs for many other applications.

■ ASSOCIATED CONTENT

Supporting Information

The Supporting Information is available free of charge at https://pubs.acs.org/doi/10.1021/jacs.3c08160.

Chemicals, instrumentation, experimental procedures, PXRD simulation data, and additional materials characterization (FT-IR, PXRD, TGA, SEM, NMR, gas sorption analysis, adsorption, and DFT calculations) (PDF)

■ AUTHOR INFORMATION

Corresponding Authors

Hui Yang − *College of Environmental Science and Engineering, North China Electric Power University, Beijing 102206, P. R. China;* orcid.org/0000-0002-6745-642X; Email: h.yang@ncepu.edu.cn

Shengqian Ma − *Department of Chemistry, University of North Texas, Denton, Texas 76201, United States;* orcid.org/0000-0002-1897-7069; Email: shengqian.ma@unt.edu

Xiangke Wang − *College of Environmental Science and Engineering, North China Electric Power University, Beijing 102206, P. R. China;* orcid.org/0000-0002-3352-1617; Email: xkwang@ncepu.edu.cn

Authors

Mengjie Hao − *College of Environmental Science and Engineering, North China Electric Power University, Beijing 102206, P. R. China*

Yinghui Xie − *College of Environmental Science and Engineering, North China Electric Power University, Beijing 102206, P. R. China*

Ming Lei − *College of Environmental Science and Engineering, North China Electric Power University, Beijing 102206, P. R. China*

Xiaolu Liu − *College of Environmental Science and Engineering, North China Electric Power University, Beijing 102206, P. R. China*

Zhongshan Chen − *College of Environmental Science and Engineering, North China Electric Power University, Beijing 102206, P. R. China*

Geoffrey I. N. Waterhouse − *School of Chemical Sciences, The University of Auckland, Auckland 1142, New Zealand;* orcid.org/0000-0002-3296-3093

Complete contact information is available at: https://pubs.acs.org/10.1021/jacs.3c08160

Author Contributions

All authors have given approval to the final version of the manuscript.

Notes

The authors declare no competing financial interest.

■ ACKNOWLEDGMENTS

We gratefully acknowledge funding support from the National Science Foundation of China (Grants U2167218; 22322603; 22276054), the Beijing Outstanding Young Scientist Program, and the Robert A. Welch Foundation (B-0027). G.I.N.W. is supported by a James Cook Research Fellowship from New

Zealand Government funding, administered by the Royal Society Te Apārangi. We thank Dr. Jie Jin (Grant U2067215) for the kind discussion, Dr. Lujia Liu from Victoria University of Wellington for kindly helping with the crystallographic analysis and discussion, and Dr. Huabing Liu's team from Beijing Limecho Technology Co., Ltd. for recording the NMR relaxometry spectra.

REFERENCES

(1) Wang, J.; Zhuang, S. Covalent organic frameworks (COFs) for environmental applications. *Coord. Chem. Rev.* **2019**, *400*, No. 213046.
(2) Ahmed, I.; Jhung, S. H. Covalent organic framework-based materials: Synthesis, modification, and application in environmental remediation. *Coord. Chem. Rev.* **2021**, *441*, No. 213989.
(3) Haug, W. K.; Moscarello, E. M.; Wolfson, E. R.; McGrier, P. L. The luminescent and photophysical properties of covalent organic frameworks. *Chem. Soc. Rev.* **2020**, *49*, 839−864.
(4) López-Magano, A.; Daliran, S.; Oveisi, A. R.; Mas-Balleste, R.; Dhakshinamoorthy, A.; Aleman, J.; Garcia, H.; Luque, R. Recent advances in the use of covalent organic frameworks as heterogenous photocatalysts in organic synthesis. *Adv. Mater.* **2023**, *35*, No. 2209475.
(5) He, T.; Zhao, Y. Covalent organic frameworks for energy conversion in photocatalysis. *Angew. Chem., Int. Ed.* **2023**, *62*, No. e202303086, DOI: 10.1002/anie.202303086.
(6) Yusran, Y.; Fang, Q.; Valtchev, V. Electroactive covalent organic frameworks: Design, synthesis, and applications. *Adv. Mater.* **2020**, *32*, No. 2002038.
(7) Sun, C.; Sheng, D.; Wang, B.; Feng, X. Covalent organic frameworks for extracting water from air. *Angew. Chem., Int. Ed.* **2023**, *62*, No. e202303378, DOI: 10.1002/anie.202303378.
(8) Nguyen, H. L. Covalent Organic frameworks for atmospheric water harvesting. *Adv. Mater.* **2023**, *35*, No. 2300018.
(9) Wang, Z.; Zhang, S.; Chen, Y.; Zhang, Z.; Ma, S. Covalent organic frameworks for separation applications. *Chem. Soc. Rev.* **2020**, *49*, 708−735.
(10) Li, Y.; Chen, W.; Xing, G.; Jiang, D.; Chen, L. New synthetic strategies toward covalent organic frameworks. *Chem. Soc. Rev.* **2020**, *49*, 2852−2868.
(11) Han, X.; Yuan, C.; Hou, B.; Liu, L.; Li, H.; Liu, Y.; Cui, Y. Chiral covalent organic frameworks: Design, synthesis and property. *Chem. Soc. Rev.* **2020**, *49*, 6248−6272.
(12) Segura, J. L.; Royuela, S.; Mar Ramos, M. Post-synthetic modification of covalent organic frameworks. *Chem. Soc. Rev.* **2019**, *48*, 3903−3945.
(13) Guan, Q.; Zhou, L. L.; Dong, Y. B. Construction of covalent organic frameworks via multicomponent reactions. *J. Am. Chem. Soc.* **2023**, *145*, 1475−1496.
(14) Sasmal, H. S.; Kumar Mahato, A.; Majumder, P.; Banerjee, R. Landscaping covalent organic framework nanomorphologies. *J. Am. Chem. Soc.* **2022**, *144*, 11482−11498.
(15) Liang, R. R.; Jiang, S. Y.; A, R. H.; Zhao, X. Two-dimensional covalent organic frameworks with hierarchical porosity. *Chem. Soc. Rev.* **2020**, *49*, 3920−3951.
(16) Deng, L.; Ding, Z.; Ye, X.; Jiang, D. Covalent organic frameworks: chemistry of pore interface and wall surface perturbation and impact on functions. *Acc. Mater. Res.* **2022**, *3*, 879−893.
(17) Yusran, Y.; Guan, X.; Li, H.; Fang, Q.; Qiu, S. Postsynthetic functionalization of covalent organic frameworks. *Natl. Sci. Rev.* **2020**, *7*, 170−190.
(18) Yang, Y.; Yu, L.; Chu, T.; Niu, H.; Wang, J.; Cai, Y. Constructing chemical stable 4-carboxyl-quinoline linked covalent organic frameworks via Doebner reaction for nanofiltration. *Nat. Commun.* **2022**, *13*, No. 2615.
(19) Ren, X. R.; Bai, B.; Zhang, Q.; Hao, Q.; Guo, Y.; Wan, L. J.; Wang, D. Constructing stable chromenoquinoline-based covalent organic frameworks via intramolecular povarov reaction. *J. Am. Chem. Soc.* **2022**, *144*, 2488−2494.
(20) Li, K.; Wong, N. K.; Strauss, M. J.; Evans, A. M.; Matsumoto, M.; Dichtel, W. R.; Adronov, A. Postsynthetic modification of a covalent organic framework achieved via strain-promoted cycloaddition. *J. Am. Chem. Soc.* **2021**, *143*, 649−656.
(21) Yang, S.; Lv, H.; Zhong, H.; Yuan, D.; Wang, X.; Wang, R. Transformation of covalent organic frameworks from n-acylhydrazone to oxadiazole linkages for smooth electron transfer in photocatalysis. *Angew. Chem., Int. Ed.* **2022**, *61*, No. e202115655, DOI: 10.1002/anie.202115655.
(22) Liao, Q.; Ke, C.; Huang, X.; Wang, D.; Han, Q.; Zhang, Y.; Zhang, Y.; Xi, K. A versatile method for functionalization of covalent organic frameworks via Suzuki-Miyaura Cross-Coupling. *Angew. Chem., Int. Ed.* **2021**, *60*, 1411−1416.
(23) Feng, J.; Zhang, Y. J.; Ma, S. H.; Yang, C.; Wang, Z. P.; Ding, S. Y.; Li, Y.; Wang, W. Fused-ring-linked covalent organic frameworks. *J. Am. Chem. Soc.* **2022**, *144*, 6594−6603.
(24) Liu, M.; Wang, Y.-R.; Ding, H.-M.; Lu, M.; Gao, G.-K.; Dong, L.-Z.; Li, Q.; Chen, Y.; Li, S.-L.; Lan, Y.-Q. Self-assembly of anthraquinone covalent organic frameworks as 1D superstructures for highly efficient CO_2 electroreduction to CH_4. *Sci. Bull.* **2021**, *66*, 1659−1668.
(25) Xu, X.; Wu, X.; Xu, K.; Xu, H.; Chen, H.; Huang, N. Pore partition in two-dimensional covalent organic frameworks. *Nat. Commun.* **2023**, *14*, No. 3360.
(26) Lyle, S. J.; Waller, P. J.; Yaghi, O. M. Covalent organic frameworks: organic chemistry extended into two and three dimensions. *Trends Chem.* **2019**, *1*, 172−184.
(27) Liu, S.; Lin, Z.; Wang, C.; Guo, J. Dual-sided symmetric crystalline orientation of covalent organic framework membranes for unidirectional anhydrous proton conduction. *Sci. China Chem.* **2022**, *65*, 2548−2557.
(28) Xing, C.; Mei, P.; Mu, Z.; Li, B.; Feng, X.; Zhang, Y.; Wang, B. Enhancing enzyme activity by the modulation of covalent interactions in the confined channels of covalent organic frameworks. *Angew. Chem., Int. Ed.* **2022**, *61*, No. e202201378.
(29) Zhai, Q. G.; Bu, X.; Zhao, X.; Li, D. S.; Feng, P. Pore space partition in metal-organic frameworks. *Acc. Chem. Res.* **2017**, *50*, 407−417.
(30) Liu, L.; Yao, Z.; Ye, Y.; Yang, Y.; Lin, Q.; Zhang, Z.; O'Keeffe, M.; Xiang, S. Integrating the pillared-layer strategy and pore-space partition method to construct multicomponent MOFs for C_2H_2/CO_2 separation. *J. Am. Chem. Soc.* **2020**, *142*, 9258−9266.
(31) Wang, Y.; Zhao, X.; Yang, H.; Bu, X.; Wang, Y.; Jia, X.; Li, J.; Feng, P. A tale of two trimers from two different worlds: a COF-inspired synthetic strategy for pore-space partitioning of MOFs. *Angew. Chem., Int. Ed.* **2019**, *58*, 6316−6320.
(32) Zhao, X.; Bu, X.; Zhai, Q. G.; Tran, H.; Feng, P. Pore space partition by symmetry-matching regulated ligand insertion and dramatic tuning on carbon dioxide uptake. *J. Am. Chem. Soc.* **2015**, *137*, 1396−1399.
(33) Zhai, Q. G.; Bu, X. H.; Mao, C. Y.; Zhao, X.; Daemen, L.; Cheng, Y. Q.; Ramirez-Cuesta, A. J.; Feng, P. Y. An ultra-tunable platform for molecular engineering of high-performance crystalline porous materials. *Nat. Commun.* **2016**, *7*, No. 13645.
(34) Ye, Y.; Ma, Z.; Lin, R. B.; Krishna, R.; Zhou, W.; Lin, Q.; Zhang, Z.; Xiang, S.; Chen, B. Pore space partition within a metal-organic framework for highly efficient C_2H_2/CO_2 separation. *J. Am. Chem. Soc.* **2019**, *141*, 4130−4136.
(35) Saiz-Lopez, A.; Plane, J. M.; Baker, A. R.; Carpenter, L. J.; von Glasow, R.; Martin, J. C.; McFiggans, G.; Saunders, R. W. Atmospheric chemistry of iodine. *Chem. Rev.* **2012**, *112*, 1773−1804.
(36) Chapman, K. W.; Chupas, P. J.; Nenoff, T. M. Radioactive iodine capture in silver-containing mordenites through nanoscale silver iodide formation. *J. Am. Chem. Soc.* **2010**, *132*, 8897−8899.
(37) Kang, H. W.; Choi, J. H.; Lee, K. R.; Park, H. S. Addition of transition metal oxides on silver tellurite glass for radioactive iodine immobilization. *J. Nucl. Mater.* **2021**, *543*, No. 152635.

https://doi.org/10.1021/jacs.3c08160
J. Am. Chem. Soc. 2024, 146, 1904−1913

(38) Pham, T. C. T.; Docao, S.; Hwang, I. C.; Song, M. K.; Choi, D. Y.; Moon, D.; Oleynikov, P.; Yoon, K. B. Capture of iodine and organic iodides using silica zeolites and the semiconductor behaviour of iodine in a silica zeolite. *Energy Environ. Sci.* **2016**, *9*, 1050−1062.
(39) Banerjee, D.; Chen, X.; Lobanov, S. S.; Plonka, A. M.; Chan, X.; Daly, J. A.; Kim, T.; Thallapally, P. K.; Parise, J. B. Iodine adsorption in metal organic frameworks in the presence of humidity. *ACS Appl. Mater. Interfaces* **2018**, *10*, 10622−10626.
(40) Zhang, X.; Maddock, J.; Nenoff, T. M.; Denecke, M. A.; Yang, S.; Schroder, M. Adsorption of iodine in metal-organic framework materials. *Chem. Soc. Rev.* **2022**, *51*, 3243−3262.
(41) Brunet, G.; Safin, D. A.; Aghaji, M. Z.; Robeyns, K.; Korobkov, I.; Woo, T. K.; Murugesu, M. Stepwise crystallographic visualization of dynamic guest binding in a nanoporous framework. *Chem. Sci.* **2017**, *8*, 3171−3177.
(42) Hu, Y. Q.; Li, M. Q.; Wang, Y.; Zhang, T.; Liao, P. Q.; Zheng, Z.; Chen, X. M.; Zheng, Y. Z. Direct observation of confined $I^-\cdots I_2\cdots I^-$ interactions in a metal-organic framework: Iodine capture and sensing. *Chem. − Eur. J.* **2017**, *23*, 8409−8413.
(43) Sava, D. F.; Chapman, K. W.; Rodriguez, M. A.; Greathouse, J. A.; Crozier, P. S.; Zhao, H.; Chupas, P. J.; Nenoff, T. M. Competitive I_2 sorption by Cu-BTC from humid gas streams. *Chem. Mater.* **2013**, *25*, 2591−2596.
(44) Hughes, J. T.; Sava, D. F.; Nenoff, T. M.; Navrotsky, A. Thermochemical evidence for strong iodine chemisorption by ZIF-8. *J. Am. Chem. Soc.* **2013**, *135*, 16256−16259.
(45) Zhang, X.; da Silva, I.; Godfrey, H. G. W.; Callear, S. K.; Sapchenko, S. A.; Cheng, Y.; Vitorica-Yrezabal, I.; Frogley, M. D.; Cinque, G.; Tang, C. C.; Giacobbe, C.; Dejoie, C.; Rudic, S.; Ramirez-Cuesta, A. J.; Denecke, M. A.; Yang, S.; Schroder, M. Confinement of iodine molecules into triple-helical chains within robust metal-organic frameworks. *J. Am. Chem. Soc.* **2017**, *139*, 16289−16296.
(46) Liu, C.; Jin, Y.; Yu, Z.; Gong, L.; Wang, H.; Yu, B.; Zhang, W.; Jiang, J. Transformation of porous organic cages and covalent organic frameworks with efficient iodine vapor capture performance. *J. Am. Chem. Soc.* **2022**, *144*, 12390−12399.
(47) Li, B.; Dong, X.; Wang, H.; Ma, D.; Tan, K.; Jensen, S.; Deibert, B. J.; Butler, J.; Cure, J.; Shi, Z.; Thonhauser, T.; Chabal, Y. J.; Han, Y.; Li, J. Capture of organic iodides from nuclear waste by metal-organic framework-based molecular traps. *Nat. Commun.* **2017**, *8*, No. 485.
(48) Dai, D.; Yang, J.; Zou, Y. C.; Wu, J. R.; Tan, L. L.; Wang, Y.; Li, B.; Lu, T.; Wang, B.; Yang, Y. W. Macrocyclic arenes-based conjugated macrocycle polymers for highly selective CO_2 capture and iodine adsorption. *Angew. Chem., Int. Ed.* **2021**, *60*, 8967−8975.
(49) Jie, K.; Zhou, Y.; Sun, Q.; Li, B.; Zhao, R.; Jiang, D. E.; Guo, W.; Chen, H.; Yang, Z.; Huang, F.; Dai, S. Mechanochemical synthesis of pillar[5]quinone derived multi-microporous organic polymers for radioactive organic iodide capture and storage. *Nat. Commun.* **2020**, *11*, No. 1086.
(50) Guo, X.; Tian, Y.; Zhang, M.; Li, Y.; Wen, R.; Li, X.; Li, X.; Xue, Y.; Ma, L.; Xia, C.; Li, S. Mechanistic insight into hydrogen-bond-controlled crystallinity and adsorption property of covalent organic frameworks from flexible building blocks. *Chem. Mater.* **2018**, *30*, 2299−2308.
(51) Guo, X.; Li, Y.; Zhang, M.; Cao, K.; Tian, Y.; Qi, Y.; Li, S.; Li, K.; Yu, X.; Ma, L. Colyliform crystalline 2D covalent organic frameworks with quasi-3D topologies for rapid I_2 adsorption. *Angew. Chem., Int. Ed.* **2020**, *59*, 22697−22705.
(52) Zhang, M.; Li, Y.; Yuan, W.; Guo, X.; Bai, C.; Zou, Y.; Long, H.; Qi, Y.; Li, S.; Tao, G.; Xia, C.; Ma, L. Construction of flexible amine-linked covalent organic frameworks by catalysis and reduction of formic acid via the Eschweiler-Clarke reaction. *Angew. Chem., Int. Ed.* **2021**, *60*, 12396−12405.
(53) Wang, P.; Xu, Q.; Li, Z.; Jiang, W.; Jiang, Q.; Jiang, D. Exceptional iodine capture in 2D covalent organic frameworks. *Adv. Mater.* **2018**, *30*, No. 1801991.
(54) Chang, J.; Li, H.; Zhao, J.; Guan, X.; Li, C.; Yu, G.; Valtchev, V.; Yan, Y.; Qiu, S.; Fang, Q. Tetrathiafulvalene-based covalent organic frameworks for ultrahigh iodine capture. *Chem. Sci.* **2021**, *12*, 8452−8457.
(55) Xie, Y.; Pan, T.; Lei, Q.; Chen, C.; Dong, X.; Yuan, Y.; Shen, J.; Cai, Y.; Zhou, C.; Pinnau, I.; Han, Y. Ionic functionalization of multivariate covalent organic frameworks to achieve an exceptionally high iodine-capture capacity. *Angew. Chem., Int. Ed.* **2021**, *60*, 22432−22440.
(56) Xie, Y.; Pan, T.; Lei, Q.; Chen, C.; Dong, X.; Yuan, Y.; Maksoud, W. A.; Zhao, L.; Cavallo, L.; Pinnau, I.; Han, Y. Efficient and simultaneous capture of iodine and methyl iodide achieved by a covalent organic framework. *Nat. Commun.* **2022**, *13*, No. 2878.
(57) Zhang, Z.; Dong, X.; Yin, J.; Li, Z. G.; Li, X.; Zhang, D.; Pan, T.; Lei, Q.; Liu, X.; Xie, Y.; Shui, F.; Li, J.; Yi, M.; Yuan, J.; You, Z.; Zhang, L.; Chang, J.; Zhang, H.; Li, W.; Fang, Q.; Li, B.; Bu, X. H.; Han, Y. Chemically stable guanidinium covalent organic framework for the efficient capture of low-concentration iodine at high temperatures. *J. Am. Chem. Soc.* **2022**, *144*, 6821−6829.
(58) He, L.; Chen, L.; Dong, X.; Zhang, S.; Zhang, M.; Dai, X.; Liu, X.; Lin, P.; Li, K.; Chen, C.; Pan, T.; Ma, F.; Chen, J.; Yuan, M.; Zhang, Y.; Chen, L.; Zhou, R.; Han, Y.; Chai, Z.; Wang, S. A nitrogen-rich covalent organic framework for simultaneous dynamic capture of iodine and methyl iodide. *Chem* **2021**, *7*, 699−714.
(59) Zhang, H.-p.; Gong, L.-l.; Yin, M.-j.; Xiong, X.-h.; Zhang, Q.-y.; Feng, X.-f.; Luo, F.; Carney, J. B.; Yue, Y. Efficient organic iodide capture by a mesoporous bimetallic-organic framework. *Cell Rep. Phys. Sci.* **2022**, *3*, No. 100830.
(60) Hao, M.; Liu, Y.; Wu, W.; Wang, S.; Yang, X.; Chen, Z.; Tang, Z.; Huang, Q.; Wang, S.; Yang, H.; Wang, X. Advanced porous adsorbents for radionuclides elimination. *EnergyChem* **2023**, *5*, No. 100101.
(61) Jiang, Y.; Jung, H.; Joo, S. H.; Sun, Q. K.; Li, C.; Noh, H. J.; Oh, I.; Kim, Y. J.; Kwak, S. K.; Yoo, J. W.; Baek, J. B. Catalyst- and solvent-free synthesis of a chemically stable Aza-Bridged Bis(phenanthroline) macrocycle-linked covalent organic framework. *Angew. Chem., Int. Ed.* **2021**, *60*, 17191−17197.

https://doi.org/10.1021/jacs.3c08160
J. Am. Chem. Soc. 2024, 146, 1904−1913